Figure S1. **a.** ^{238}U decay series. The final decay product of the series is ^{206}Pb. **b.** ^{235}U decay series, with the final decay product of ^{207}Pb. The decay chains result from successive radioactive decay of intermediate nuclides in the series. Colored numbers indicate the half-lives of the corresponding nuclides (after Faure and Mensing, 2005). **c.** Diagram illustrating changes in parent-daughter activity ratios for the nuclides discussed in this review. Activity ratios decay over different timescales as a result of the differing half-lives of the daughter nuclides shown.

Figure S2. ($^{231}Pa/^{235}U$) vs. $^{176}Hf/^{177}Hf$ data for Iceland, with selected sample data and dynamic melting model calculations after Koornneef et al. (2012). One set of calculated binary mixtures between chemically and thermally isolated melts of depleted peridotite and enriched pyroxenite sources is also shown (Koornneef et al., 2012). Tick marks for peridotite and pyroxenite melts indicate the calculated composition of each partial melt at a given pressure of melting along a single 1D column. Tick marks along the dashed binary mixing line indicate the proportions of melt contributed from each source for a single calculated extraction depth of 0.9 GPa. Based on the limited $^{176}Hf/^{177}Hf$ isotopic range observed in the selected Icelandic basalts, the proportion of melt contributed by partial melting of the pyroxenite source can be quantitatively constrained to less than 10% (Koornneef et al., 2012). Given an assumed pyroxenite composition and melt fertility, it is possible to further constrain the percentage of pyroxenite present in the unmelted Icelandic source region.

Figure S3. Gridded results of time-dependent dynamic melting model calculations, for T_p = 1300ºC, final melting pressure of 0.5 GPa, and peridotite and pyroxenite in thermal equilibrium, across a range of solid mantle upwelling (W; solid lines) and maximum residual melt porosity (ϕ) values (dashed lines). Data fields indicate global MORB data after Figure 3. Panels show results for **a.** ($^{226}Ra/^{230}Th$) and **b.** ($^{231}Pa/^{235}U$) vs. ($^{230}Th/^{238}U$) in partial melts of peridotite in

thermal equilibrium with Gb-108 pyroxenite, **c.** ($^{226}Ra/^{230}Th$) and **d.** ($^{231}Pa/^{235}U$) vs. ($^{230}Th/^{238}U$) in partial melts of Gb-108 pyroxenite, **e.** ($^{226}Ra/^{230}Th$) and **f.** ($^{231}Pa/^{235}U$) vs. ($^{230}Th/^{238}U$) in partial melts of peridotite in thermal equilibrium with MIX-1G pyroxenite, and **g.** ($^{226}Ra/^{230}Th$) and **h.** ($^{231}Pa/^{235}U$) vs. ($^{230}Th/^{238}U$) in partial melts of MIX-1G pyroxenite.

Figure S4. Gridded results of time-dependent dynamic melting model calculations, for T_p = 1550ºC, final melting pressure of 0.5 GPa, and peridotite and pyroxenite in thermal equilibrium, across a range of solid mantle upwelling (W) and maximum residual melt porosity (ϕ) values and with panels as in Figure S3. Data fields indicate global OIB data after Figure 4.

Figure S5. Gridded results of time-dependent RPF melting calculations, for T_p = 1300ºC, final melting pressure of 0.5 GPa, and peridotite and pyroxenite in thermal equilibrium, across a range of solid mantle upwelling (W) and maximum residual melt porosity (ϕ) values and with panels and fields as in Figure S3.

Figure S6. Gridded results of time-dependent RPF melting calculations, for T_p = 1550ºC, final melting pressure of 0.5 GPa, and peridotite and pyroxenite in thermal equilibrium, across a range of solid mantle upwelling (W) and maximum residual melt porosity (ϕ) values and with panels and fields as in Figure S4.

Figure S7. Gridded results of time-dependent RPF melting calculations, for T_p = 1550ºC, final melting pressure of 2.0 GPa, and peridotite and pyroxenite in thermal equilibrium, across a range of solid mantle upwelling (W) and maximum residual melt porosity (ϕ) values and with panels and fields as in Figure S4.

Figure S8. Gridded results of time-dependent dynamic melting calculations, for T_p = 1550ºC, final melting pressure of 2.0 GPa, and peridotite and pyroxenite in thermal equilibrium, across a range of solid mantle upwelling (W) and maximum residual melt porosity (ϕ) values and with panels and fields as in Figure S4.

Figure S9. Gridded results of time-dependent dynamic melting model calculations, for T_p = 1300ºC, final melting pressure of 0.5 GPa, and thermally isolated peridotite and pyroxenite, across a range of solid mantle upwelling (W) and maximum residual melt porosity (ϕ) values. Data fields are as in Figure S3. Panels show results for **a.** ($^{226}Ra/^{230}Th$) and **b.** ($^{231}Pa/^{235}U$) vs. ($^{230}Th/^{238}U$) in partial melts of peridotite, **c.** ($^{226}Ra/^{230}Th$) and **d.** ($^{231}Pa/^{235}U$) vs. ($^{230}Th/^{238}U$) in partial melts of Gb-108 pyroxenite, and **e.** ($^{226}Ra/^{230}Th$) and **f.** ($^{231}Pa/^{235}U$) vs. ($^{230}Th/^{238}U$) in partial melts of MIX-1G pyroxenite.

Figure S10. Gridded results of time-dependent dynamic melting model calculations, for T_p = 1550ºC, final melting pressure of 0.5 GPa, and thermally isolated peridotite and pyroxenite, across a range of solid mantle upwelling (W) and maximum residual melt porosity (ϕ) values and with panels and fields as in Figure S4.

Figure S11. Gridded results of time-dependent RPF melting model calculations, for T_p = 1300ºC, final melting pressure of 0.5 GPa, and thermally isolated peridotite and pyroxenite, across a range of solid mantle upwelling (W) and maximum residual melt porosity (ϕ) values and with panels and fields as in Figure S3.

Figure S12. Gridded results of time-dependent RPF melting model calculations, for T_p = 1550ºC, final melting pressure of 0.5 GPa, and thermally isolated peridotite and pyroxenite,

across a range of solid mantle upwelling (W) and maximum residual melt porosity (ϕ) values and with panels and fields as in Figure S4.

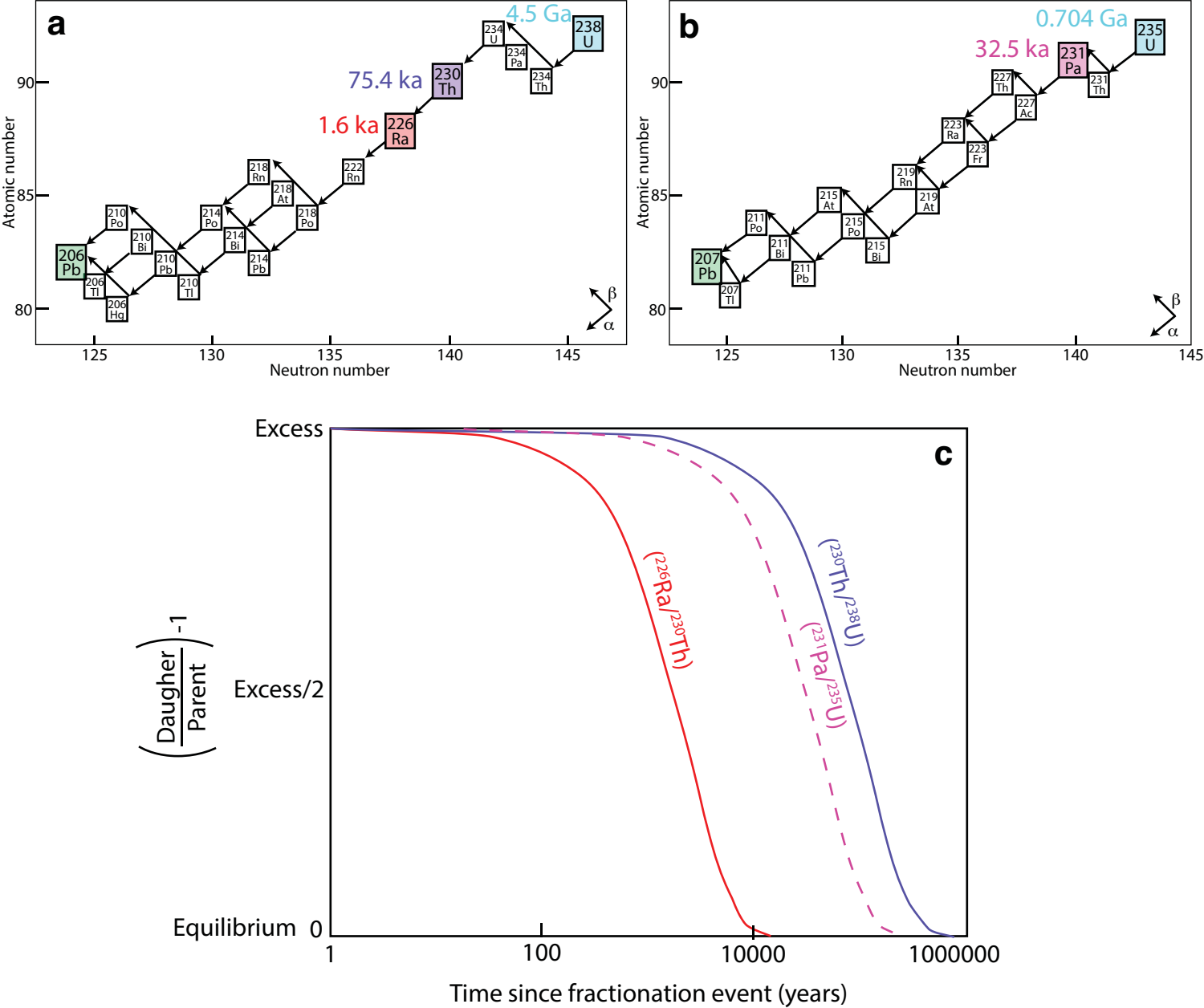
a
4.5 Ga
75.4 ka
1.6 ka
238 U
234 U
234 Pa
234 Th
230 Th
226 Ra
222 Rn
218 Rn
218 At
218 Po
214 Po
214 Bi
214 Pb
210 Po
210 Bi
210 Pb
210 Tl
206 Pb
206 Tl
206 Hg
Atomic number
Neutron number
90
85
80
125
130
135
140
145
β
α
b
0.704 Ga
32.5 ka
235 U
231 Pa
231 Th
227 Th
227 Ac
223 Ra
223 Fr
219 Rn
219 At
215 At
215 Po
215 Bi
211 Po
211 Bi
211 Pb
207 Pb
207 Tl
c
Excess
Excess/2
Equilibrium
0
1
100
10000
1000000
Time since fractionation event (years)
(Daugher/Parent) -1
(226Ra/230Th)
(230Th/238U)
(231Pa/235U)

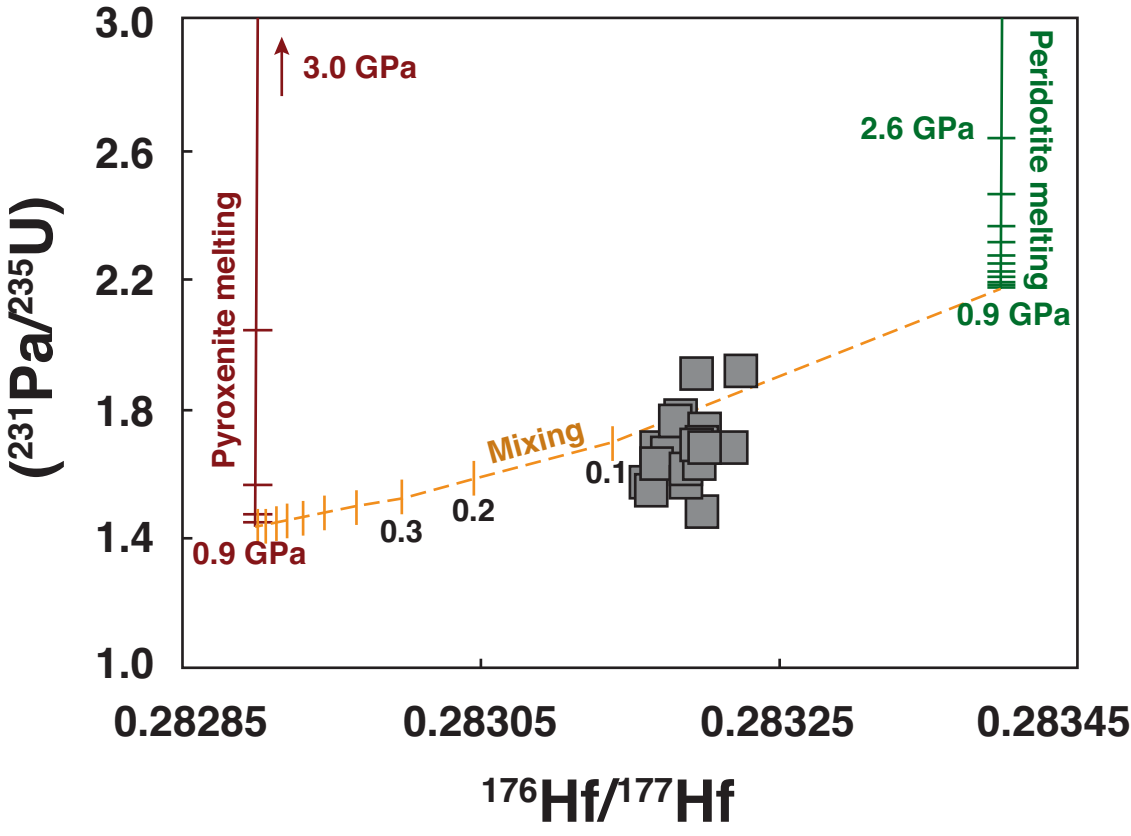
3.0
2.6
2.2
1.8
1.4
1.0
0.28285
0.28305
0.28325
0.28345
$^{176}Hf/^{177}Hf$
$(^{231}Pa/^{235}U)$
3.0 GPa
Pyroxenite melting
0.9 GPa
Mixing
0.3
0.2
0.1
2.6 GPa
Peridotite melting
0.9 GPa

T_p = 1300°C, lithologies in thermal equilibrium
Final melting pressure = 0.5 GPa
Dynamic melting

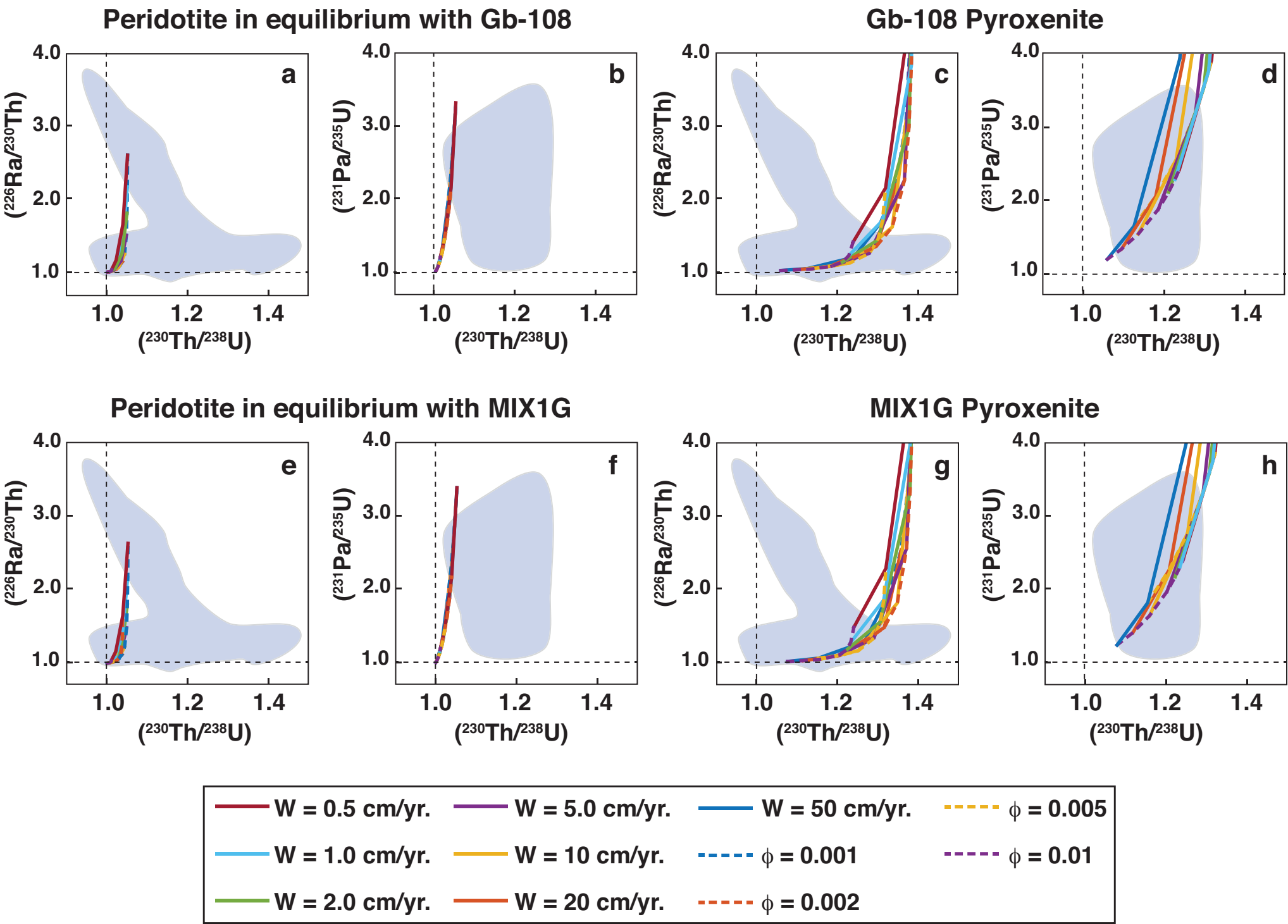

T_p = 1550°C, lithologies in thermal equilibrium
Final melting pressure = 0.5 GPa
Dynamic melting

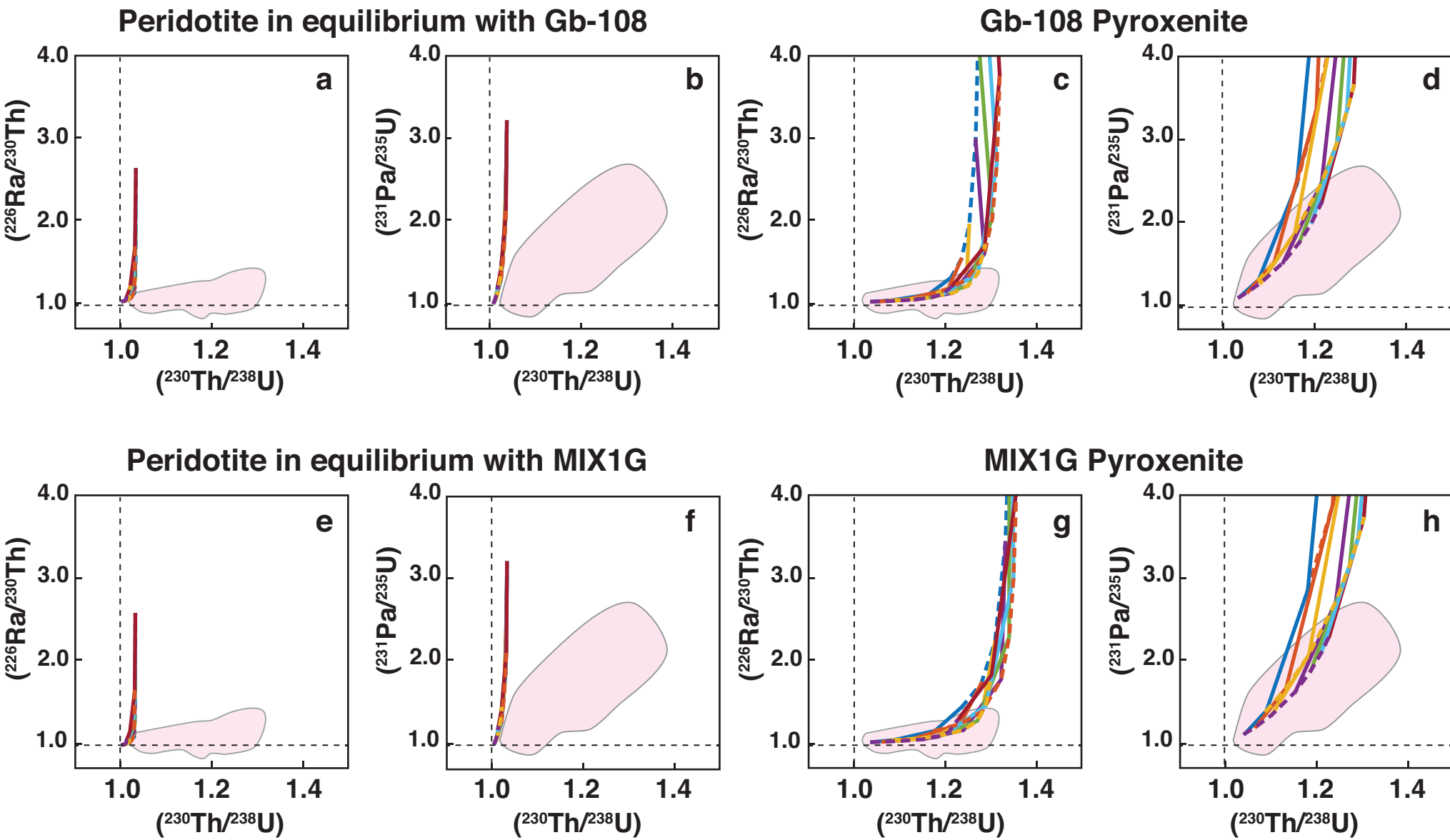

T_p = 1300°C, lithologies in thermal equilibrium
Final melting pressure = 0.5 GPa
Reactive porous flow melting

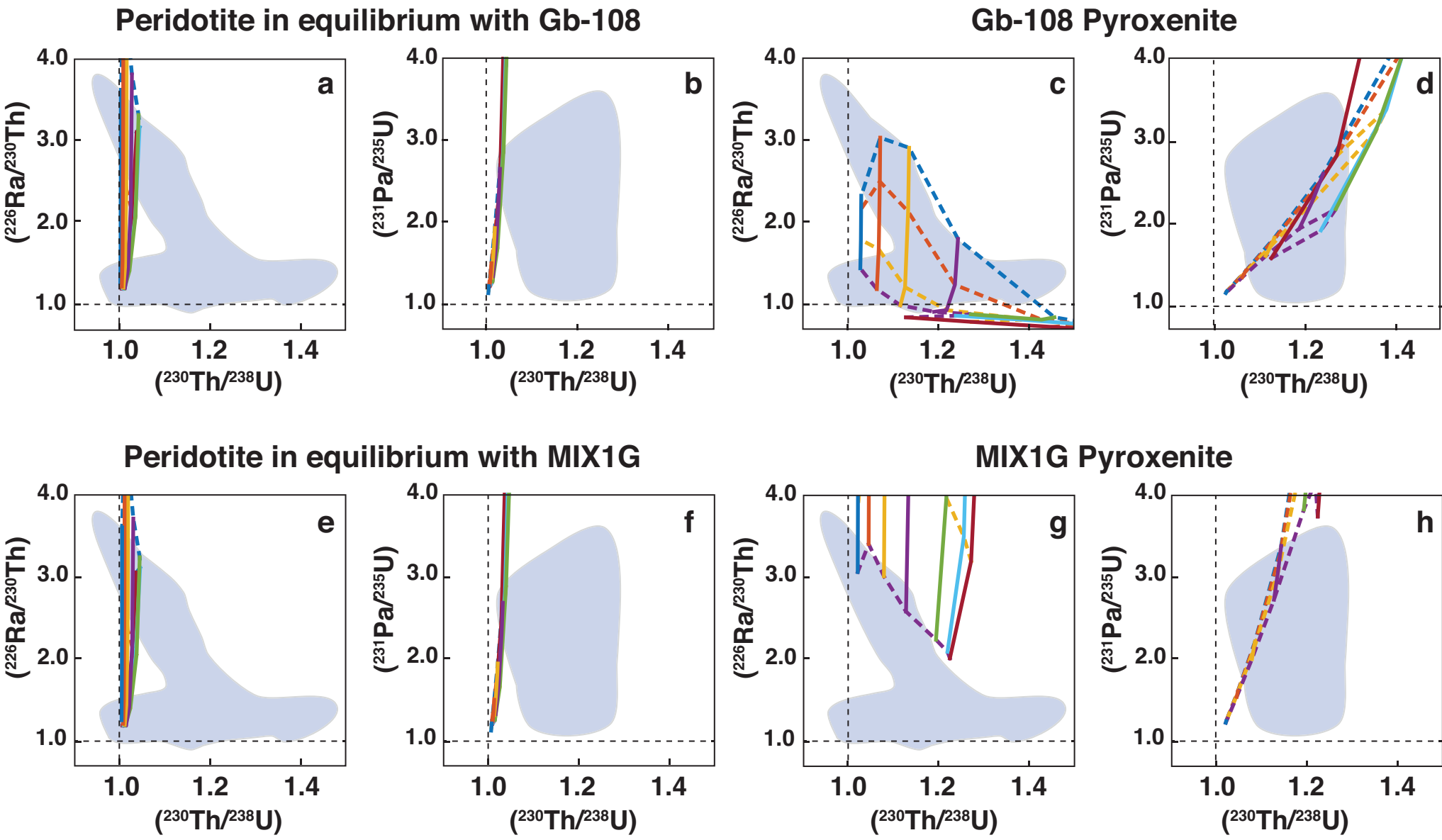

T_p = 1550°C, lithologies in thermal equilibrium
Final melting pressure = 0.5 GPa
Reactive porous flow melting

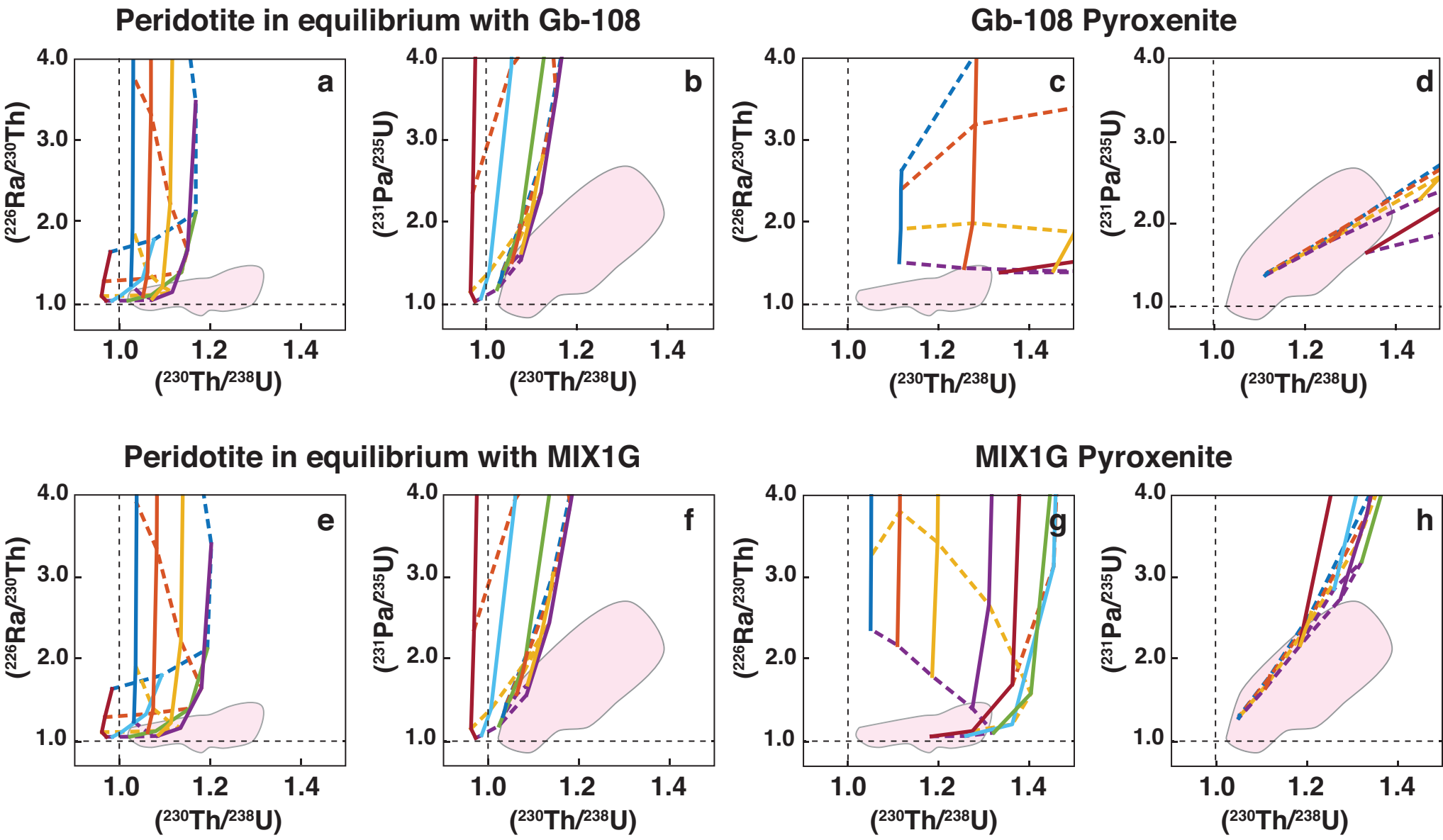

T_p = 1550°C, lithologies in thermal equilibrium
Final melting pressure = 2.0 GPa
Reactive porous flow melting

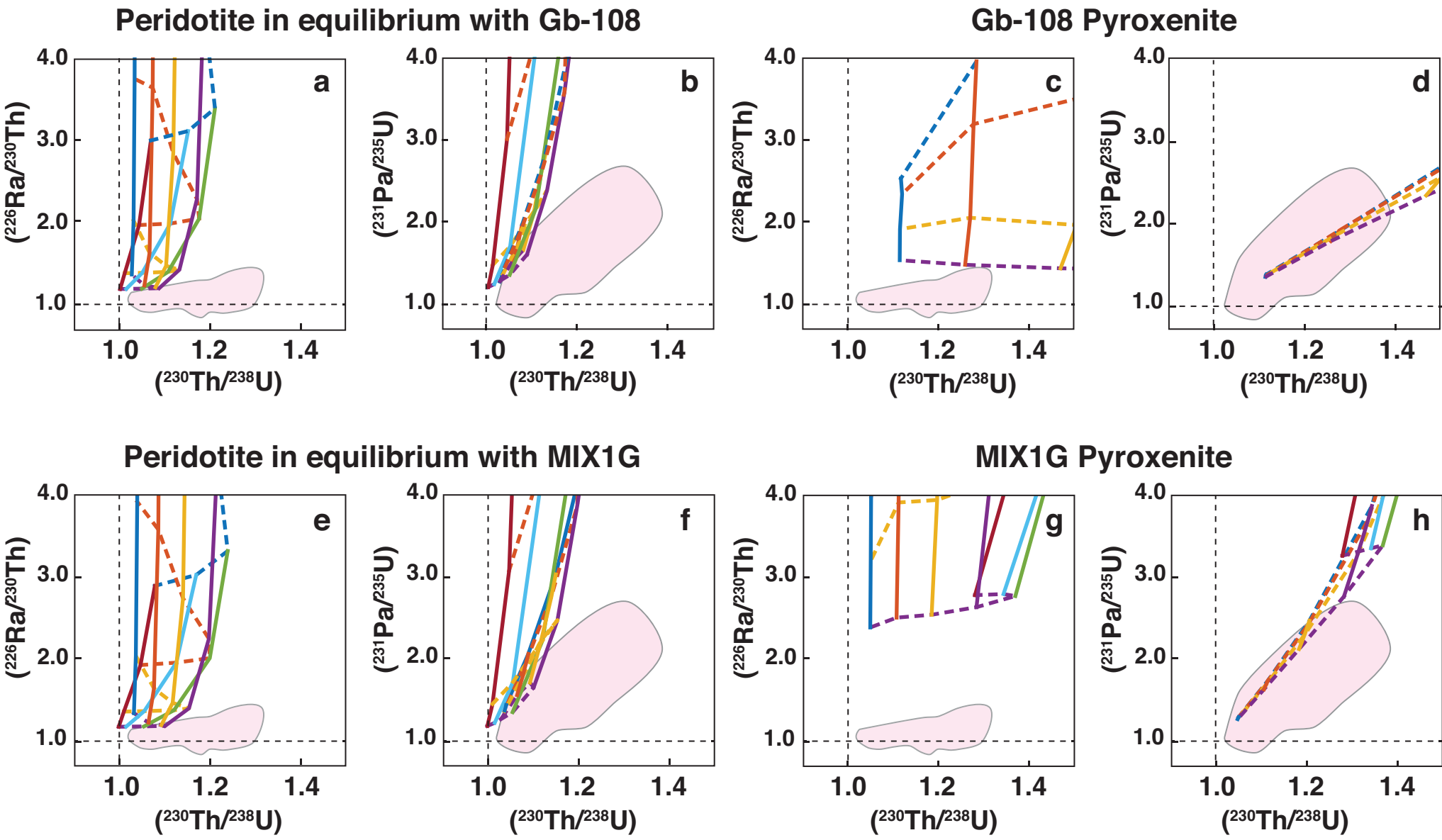

T_p = 1550°C, lithologies in thermal equilibrium
Final melting pressure = 2.0 GPa
Dynamic melting

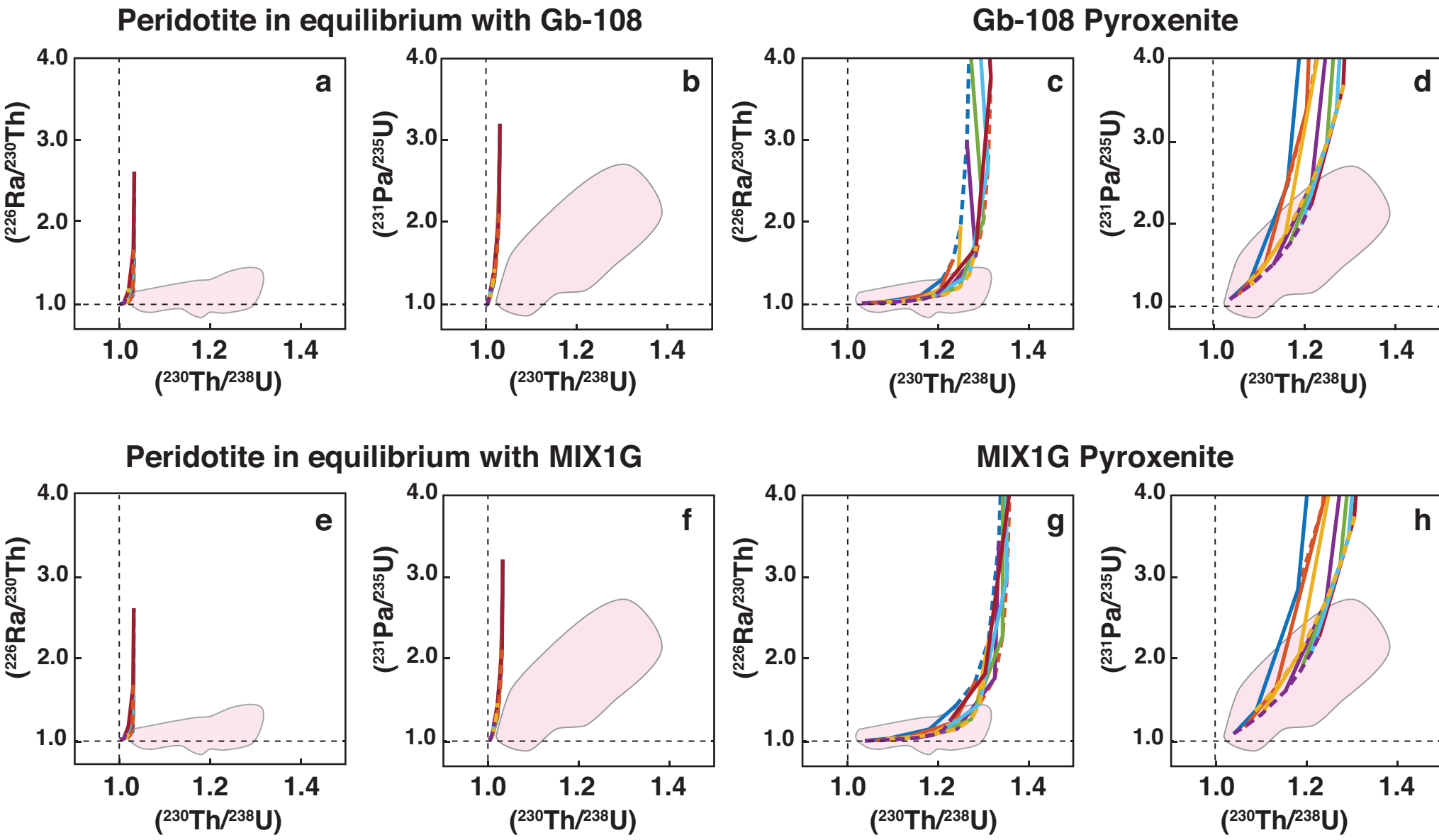

T_p = 1300°C, lithologies in thermal isolation
Final melting pressure = 0.5 GPa
Dynamic melting

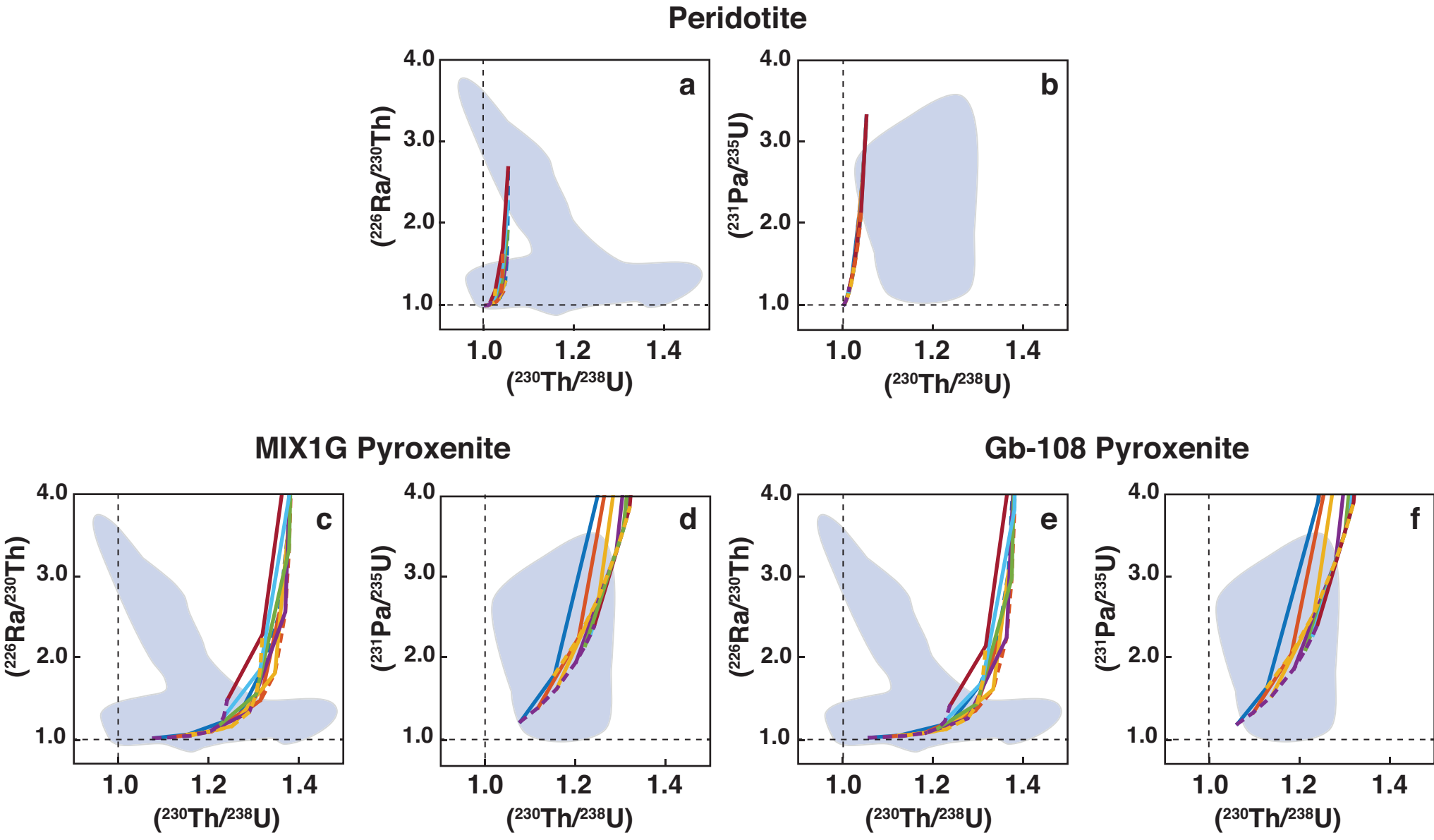

T_p = 1550°C, lithologies in thermal isolation
Final melting pressure = 0.5 GPa
Dynamic melting

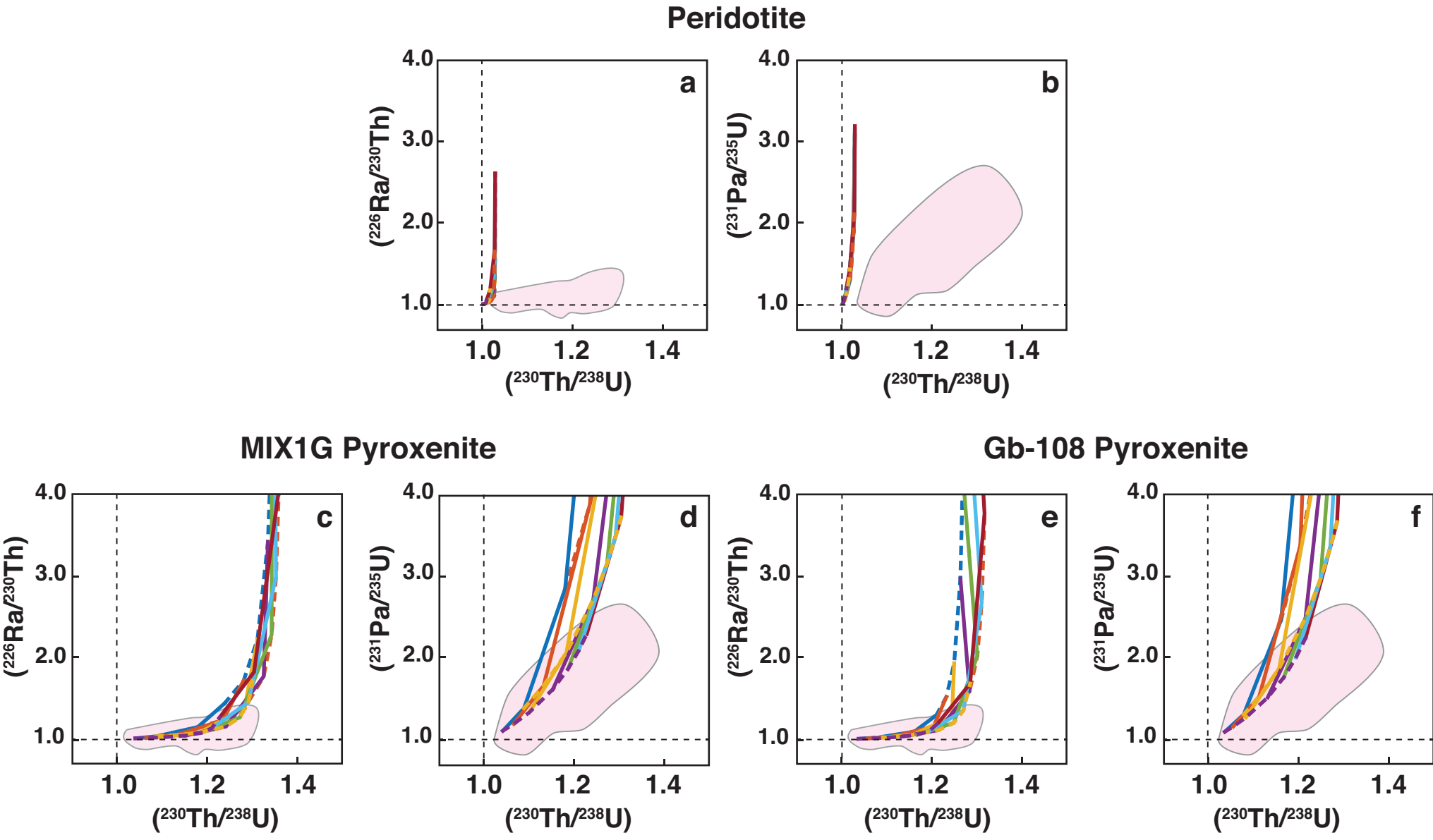

T_p = 1300°C, lithologies in thermal isolation
Final melting pressure = 0.5 GPa
Reactive porous flow melting

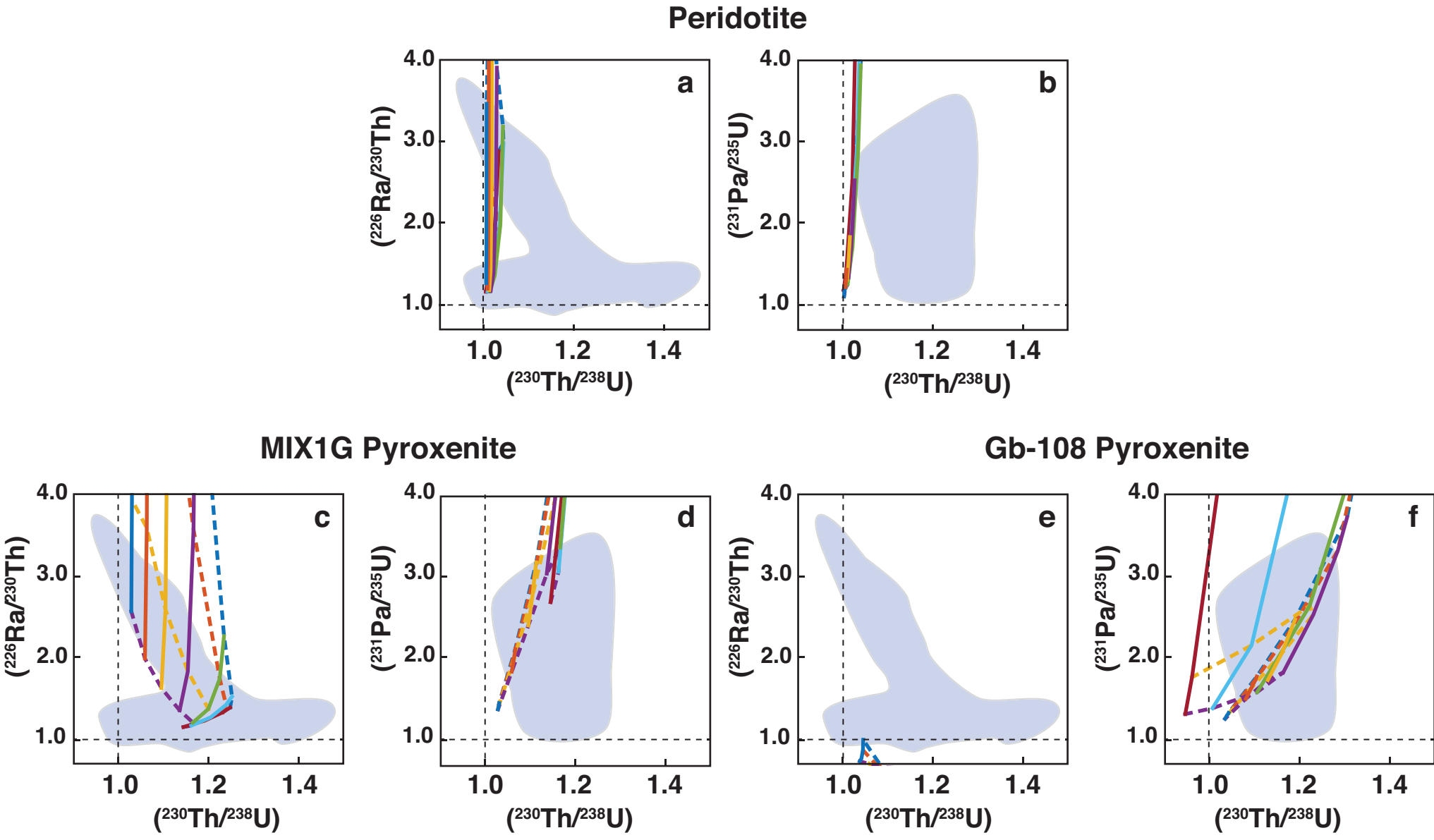

T_p = 1550°C, lithologies in thermal isolation
Final melting pressure = 0.5 GPa
Reactive porous flow melting